

Communication

# Design of a Large Field of View and Low-Distortion Off-Axis Optical System Based on a Free-Form Surface

Bing Jia <sup>1,2</sup>, Yubing Li <sup>1,\*</sup> , Qiongying Lv <sup>1</sup>, Fan Jin <sup>1</sup> and Chunlin Tian <sup>1</sup>

<sup>1</sup> College of Mechanical and Electrical Engineering, Changchun University of Science and Technology, Changchun 130022, China; 2015800071@cust.edu.cn (B.J.)

<sup>2</sup> Chongqing Research Institute, Changchun University of Science and Technology, Chongqing 401120, China

\* Correspondence: 13304456182@163.com; Tel.: +86-13304456182

**Abstract:** Free-form surfaces have good aberration correction capability and balance capability for nonrotationally symmetric imaging systems. In this study, we analyzed the quantitative relationship between  $X$ - $Y$  polynomial combination and aberration for the efficient design of  $X$ - $Y$  free-form optical systems. The purpose of this study was to provide an exhaustive design method for off-axis triple inverse optical systems with  $X$ - $Y$  free-form surfaces. Finally, we designed a free-form off-axis optical system with a large field of view (FOV) and low distortion based on the off-axis triple inverse optical system without an intermediate image plane. The primary mirror (PM) of the system adopted an  $X$ - $Y$  polynomial free-form surface to correct the aberration of different FOVs of the system and improve the image width and quality. The optical system had a focal length of 1000 mm, an  $F$ -value of 9.5, an FOV angle of  $23^\circ \times 1^\circ$ , a maximum distortion grid in the FOV less than or equal to  $-0.05\%$ , and a full-field average wave aberration better than  $0.055 \lambda$  ( $\lambda/18.2$ ,  $\lambda = 632.8$  nm). The analysis of the design results showed that the system had high-quality imaging and a compact structure. This design method can provide a technical reference for the study of such free-form off-axis systems.

**Keywords:** optical design; off-axis three mirrors; free-form surface; distortion; tolerance analysis



**Citation:** Jia, B.; Li, Y.; Lv, Q.; Jin, F.; Tian, C. Design of a Large Field of View and Low-Distortion Off-Axis Optical System Based on a Free-Form Surface. *Photonics* **2023**, *10*, 506.

<https://doi.org/10.3390/photonics10050506>

Received: 17 March 2023

Revised: 21 April 2023

Accepted: 24 April 2023

Published: 27 April 2023



**Copyright:** © 2023 by the authors. Licensee MDPI, Basel, Switzerland. This article is an open access article distributed under the terms and conditions of the Creative Commons Attribution (CC BY) license (<https://creativecommons.org/licenses/by/4.0/>).

## 1. Introduction

With the rapid development of advanced precision optics, optical imaging systems with high resolution, large field of view (FOV) and wide spectral range have become the new development trend [1–3]. A three-mirror anastigmat system (TMAS) is a reflective optical system that evolved from a three-mirror coaxial system (TMCS) by biasing the FOV or aperture. The TMAS has received an increasing amount of attention in the domain of optical remote sensing because the system has the characteristics of long focal length, no chromatic aberration, good thermal performance, and comprehensive spectral band coverage. Thus, the TMAS has the advantages of a larger FOV and better imaging quality [4,5]. TMASs have been widely used in many international remote sensing optical systems, such as SPOT-6, Worldview-1, ALOS-3, PROB-V, and GOCI [6–9].

The TMAS avoids the central occlusion of the TMCS and improves the imaging quality. At the same time, the system loses its rotational symmetry, leading to a dramatic increase in advanced aberration of off-axis FOV. For large FOV optical systems using linear array push-scan mode imaging, aberrations in the push-scan direction can cause image shift, which leads to blurred imaging and reduces the imaging quality of the system [10,11]. However, it is challenging for off-axis reflective optical systems with conventional spherical or nonspherical shapes to balance large FOV, low distortion, and system modulation transfer function (MTF) because of the design degrees of freedom (DOF). Therefore, understanding how to increase the system FOV, reduce aberrations, and ensure a compact system structure with high-quality imaging has become an urgent problem in space optical systems.

Free-form surfaces, which rely on manufacturing and inspection technology developments, provide an excellent solution to meet the increasingly demanding performance

specifications and large FOV requirements of optical systems [12–14]. The free-form surface is widely used in panoramic optical systems, head-mounted displays, and off-axis reflective optical systems [15–17]. Free-form optics are optical surfaces with nonrotationally symmetric characteristics that can improve optical performance while enabling more novel features, reducing the size of rotationally asymmetric optical systems, and correcting system aberrations [18–20]. To date, the main parametric representations for optical free-form design include  $X$ – $Y$  polynomials, Zernike polynomials, Q-polynomials, radial basis functions, and spline functions [21].  $X$ – $Y$  polynomial surfaces and Zernike polynomial surfaces have the same free-form surface characterization capability, have interconversion relationships, and are more often used in machining [22]. In recent years, an increasing number of research institutions have launched corresponding studies on the spatial application of free-form surfaces. For example, the imaging spectrometer developed by the Institute of Optics at the University of Rochester takes advantage of the compactness of the free-form surface structure, reducing the size of the optical system by a factor of five compared with those using conventional spherical or aspheric designs, while expanding the spatial spread by a factor of two [23]. The free-form spatial off-axis reflective optical system developed by the Changchun Institute of Optics, Fine Mechanics, and Physics of the Chinese Academy of Sciences, has achieved  $76^\circ$  FOV imaging [24]. The free-form off-axis triple inverted infrared imaging system developed by Tsinghua University and Tianjin University takes advantage of the free-form design to greatly reduce the difficulty of mounting the system, which has a focal length of 138 mm and an FOV of  $4^\circ \times 5^\circ$  and works in the medium-wave and long-wave infrared wavelengths [16].

In this study, we proposed a large FOV and low-distortion TMAS based on an  $X$ – $Y$  polynomial and described the method used to achieve this system. Compared to TMAS using conventional spherical or aspheric surface shapes, this system used the free-form surface to expand the design freedom of the system and to further improve the aberration balance capability of the system. Although the loss of rotational symmetry makes the measurement and processing of free-form surfaces challenging, the increasing sophistication of computer inspection technology and optical precision machining techniques have made it possible to fabricate components for imaging systems with larger free-form surfaces. This system has a certain reference value for designing a space optical system. It is suitable for a large FOV and low-distortion linear array push-broom imaging optical system. The remainder of this paper is organized as follows: In Section 2, the optical design, considerations, and initial configurations of the TMAS are described. In Section 3, the quantitative relationship between the  $X$ – $Y$  polynomial, the Fringe Zernike polynomial, and the aberration is analyzed. In Section 4, a design example of a TMAS with a focal length of 1000 mm, an F-value of 9.5, a large FOV of  $23^\circ \times 1^\circ$ , and a distortion of less than 0.05% is given, and the imaging quality and tolerance of the system are analyzed. Section 5 discusses the results.

## 2. Optical System Design

The classic method of establishing the structure of the reflective optical system is based on the theory of near-axis optics, solving the structural parameters of the coaxial optical system using primary aberration theory, and then eliminating the central occlusion by FOV off-axis or aperture off-axis to establish the initial structure. The initial configuration of a TMAS evolved from a TMCS, a biased aperture, and FOV, and we adopted this configuration to eliminate the obstruction. The TMCS initial structure parameters include eight parameters: the radius of three surfaces, namely  $R_1$ ,  $R_2$ , and  $R_3$ ; the distance from the primary mirror (PM) to the secondary mirror (SM) is  $d_1$ ; the distance from the SM to the tertiary mirror (TM) is  $d_2$ ; and the quadratic surface coefficients of the three mirrors are  $K_1$ ,  $K_2$ , and  $K_3$ . To simplify the process of solving the initial structural parameters, the PM and TM of the optical system overlapped when  $d_1 = d_2$ . The initial configuration of the TMCS that was used in this study is shown in Figure 1. The calculation method for the initial

configuration of the TMCS was based on the third-order aberration theory, which has been introduced in many literature references [25–27] and is not discussed in detail here.

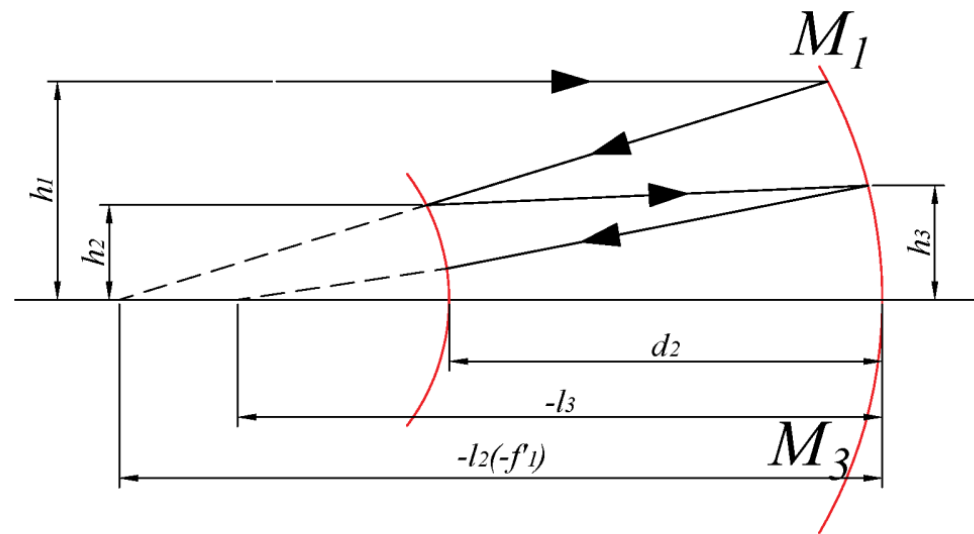


Figure 1. Initial TMCS configuration.

Two common forms of TMAS are applied in the optical remote sensing domain: relayed TMAS, shown in Figure 2a, and nonrelayed TMAS, shown in Figure 2b.

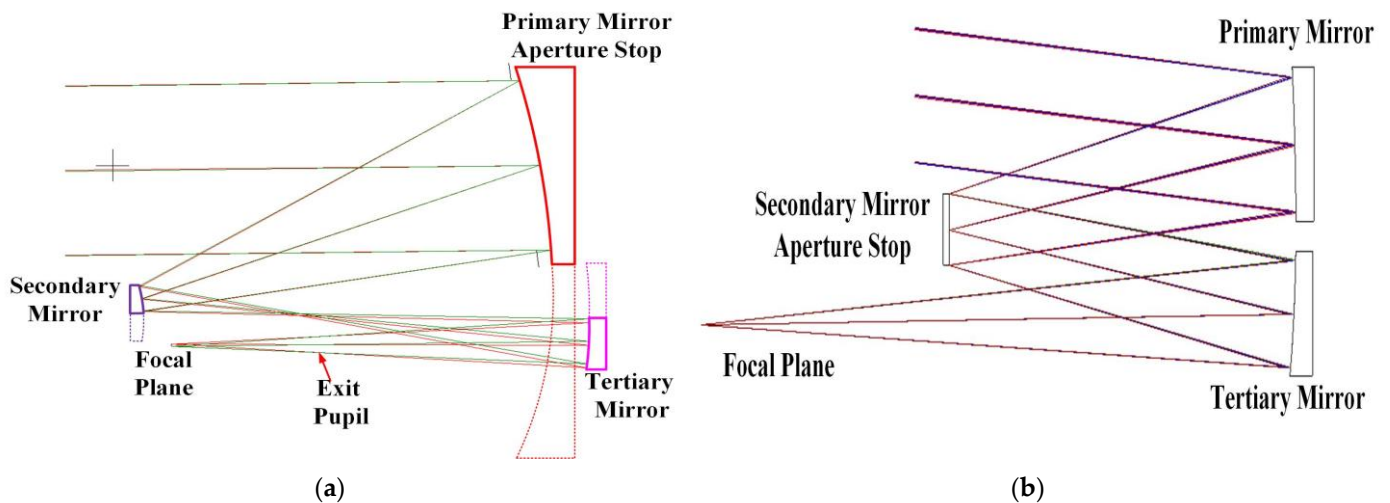


Figure 2. (a) Relayed TMAS; and (b) nonrelayed TMAS.

In a relayed TMAS [28], shown in Figure 2a, the aperture stop is located at the PM or the entrance pupil of the system. Because the system is the off-axis part of the TMCS, it inherits the advantage of the highly compact ratio of the TMCS. It has an intermediate imaging plane between the SM and the TM, and a real exit pupil in the back focal length (BFL). These places are suitable for a field stop and a rear stop, which can ensure that the system has good performance in the suppression of stray radiation. Because of the real exit pupil, the system is also suitable for multispectral imaging with a common aperture. However, because the relayed TMAS inherited the configurable characteristics of the TMCS, it has been difficult to achieve a large FOV.

In a nonrelayed TMAS [29], shown in Figure 2b, the aperture stop is located at the SM, and a biased FOV is adopted to remove the obstruction of the SM. However, because the biased FOV moves the real FOV away from the field center, more nonsymmetric aberrations are generated when the biased angle increases. The PM and the TM are symmetrically

relative to the optical axis, similar to the projection of the subpupil of each FOV. As a result, forms of the PM and TM are usually rectangular with high aspect ratios (ARs). This configuration is beneficial to lateral aberration correcting and larger FOV imaging. As the FOV increases, however, the aspect ratio of the PM and TM will gradually increase.

In contrast to a relayed TMAS, a nonrelayed TMAS can easily implement large FOV imaging, and it is more suitable for optical remote sensing with a drift-scan pattern. At the same time, a rectangular mirror manufactured with metal can achieve a low surface shape error with a much higher lightweight level, which can make up for the deficiency in size and weight of a nonrelayed TMAS. Therefore, in this study, we adopted a nonrelayed TMAS for the initial configuration to further optimize the large FOV and the low-distortion TMAS.

### 3. Quantitative Analysis of the Free-Form Surface

A free-form surface is a nonrotationally symmetrical optical surface type. Compared with conventional spherical and aspherical surfaces, a free-form surface can offer more DOFs for optical designers and enhance the corrective abilities of an off-axis aberration. This type of optical imaging system mainly uses Zernike polynomials and X–Y polynomials [30]. An X–Y polynomial was first used for low-order free-form surfaces and most commonly is used to describe free-form surfaces. An X–Y polynomial adds a more refined shape description to a surface sag as well as more effective DOFs for higher-order aberration correction. An X–Y polynomial is also a classic nonorthogonal polynomial that is suitable for three-dimensional modeling and numerically controlled optical manufacturing. Because it can achieve high precision in mirror shape, it is widely used in metal-based mirrors, such as the JSS-56 imager [31]. The expression of the X–Y polynomial is as follows:

$$Z = \frac{cr^2}{1 + \sqrt{1 - (1 + k)c^2r^2}} + \sum_{i=1}^N A_i E_i(x, y) \tag{1}$$

where  $Z$  is the sag of the surface parallel to the  $z$ -axis,  $c$  is the vertex curvature,  $r$  is the radial coordinate,  $k$  is the conic constant,  $N$  is the polynomial sequence,  $A_i$  is the polynomial coefficient, and  $E_i(x, y)$  is the polynomial-like difference term expression.

A Zernike polynomial is a complete set of functions that is orthogonal over a circle with a unit radius. This characteristic makes it much more suitable for describing and fitting an aberration. A fringe Zernike polynomial has a uniform equation and uniform characteristics, except that the terms of the Fringe Zernike are remapped according to an interferometric data analysis program. Thus, the Fringe Zernike is widely used in the design, detection, and alignment of optical systems. The expression of the Zernike polynomial is as follows:

$$Z = \frac{cr^2}{1 + \sqrt{1 - (1 + k)c^2r^2}} + \sum_{j=1}^N C_{(j+1)} ZP_j \tag{2}$$

where  $C_{(j+1)}$  is the polynomial coefficient and  $ZP_j$  is the polynomial-like difference term expression.

As seen in Equation (1), the X–Y polynomial is usually expressed in Cartesian coordinates. The X–Y polynomial is consistent with the computer numerical control machine expression and is highly practical for the machining of metal reflectors [32]. Because the free-form surface corresponds to a specific geometric aberration, it has a more powerful off-axis field aberration correction capability. The design of an optical imaging system involves the process of an aberration balance to produce the minimum residual wavefront error (WFE). Optimization of optical systems using X–Y polynomials is to obtain better free-form surface solutions by solving for the coefficients of each order, which in turn optimizes the system aberration to improve the imaging quality. As expressed by Equation (2), the Zernike polynomial is usually expressed in polar coordinates. The Zernike polynomial corresponds with the geometric aberration, which can describe the aberration of the system

more easily. Thus, this translates into the problem of solving the relationship between the X–Y polynomial and the Fringe Zernike polynomial.

To better illustrate the relationship between the X–Y polynomial and the aberration, we converted each aberration term in the Fringe Zernike polynomial to a Cartesian coordinate system, and the conversion equation is shown in Equation (3).

$$\begin{aligned} X &= R \times \cos\theta \\ Y &= R \times \sin\theta' \end{aligned} \tag{3}$$

where  $R$  is the radial distance and  $\theta$  is the azimuth angle.

Different X–Y polynomial combinations are added to the single parabolic mirror surface to characterize the aberrations in the transformed Fringe Zernike polynomials. This method is used to verify the aberration correction ability of the X–Y polynomial. We analyzed only third-order aberrations, and the aberration results are shown in Table 1.

**Table 1.** Coordinate transformation.

No.	Aberration	Radial Coordinate	Cartesian Coordinate
1	Piston	1	1
2	Tilt (X)	$R\cos\theta$	X
3	Tilt (Y)	$R\sin\theta$	Y
4	Defocus	$2R^2 - 1$	$2X^2 + 2Y^2 - 1$
5	Astig (0°)	$R^2\cos(2\theta)$	$X^2 - Y^2$
6	Astig (45°)	$R^2\sin(2\theta)$	2XY
7	Coma (X)	$(3R^3 - 2R)\cos\theta$	$3X^3 + 3XY^2 - 2X$
8	Coma (Y)	$(3R^3 - 2R)\sin\theta$	$3X^2Y + 3Y^3 - 2Y$
9	Spherical	$6R^4 - 6R^2 + 1$	$6X^4 + 12X^2Y^2 + 6Y^4 - 6X^2 - 6Y^2 + 1$
10	Trefoil (X)	$R^3\cos(3\theta)$	$X^3 - 3XY^2$
11	Trefoil (Y)	$R^3\sin(3\theta)$	$3X^2Y - Y^3$

The analysis and results of the relationship between the combination of X–Y polynomials and each of the aberrations using the specified approach revealed the following: (1) The sign of the monomial only affected the value of the aberration, without affecting the type of aberration, and the variation in the coefficient of  $A_{ij}$  led to an absolute value change in the aberration. (2) In the polynomial combinations used to represent the different aberrations, the sign of various monomials affected the types of aberration. Considering items 4 and 5 in Table 2 as an example, when  $A_{02}$  had a positive value, the system was defocused. The wavefront aberration map for this scenario is shown in Figure 3a. When  $A_{02}$  had a negative value, the system had an astigmatism. The wavefront aberration map for this scenario is shown in Figure 3b. (3) The combination of X–Y polynomials, when characterizing a particular aberration, also produced other aberration terms, but the magnitude of the other aberration terms usually was small.

**Table 2.** Relationship between X–Y polynomial and Fringe Zernike polynomial.

No.	Aberrations	Coefficient	Value	X–Y Polynomial Combinations	Coefficient	Value
1	Piston	0	0	0	0	0
2	Tilt (X)	0	0	$A_{10}$	0	0
3	Tilt (Y)	0	0	$A_{01}$	0	0
4	Defocus	$1 \times 10^{-3}$	−6.3209	$2A_{20} + 2A_{02}$	$1 \times 10^{-3}$	Piston: −3.1605 Defocus: −3.129
5	Astig (0°)	$1 \times 10^{-3}$	−3.1531	$A_{20} - A_{02}$	$1 \times 10^{-3}$	−3.1534
6	Astig (45°)	$1 \times 10^{-3}$	−3.1530	$2A_{11}$	$1 \times 10^{-3}$	−3.1528
7	Coma (X)	$1 \times 10^{-3}$	Tilt(X): −6.322 Coma(X): −3.105	$3A_{30} + 3A_{12} - 2A_{10}$	$1 \times 10^{-3}$	Tilt(X): −6.322 Coma(X): −3.105
8	Coma (Y)	$1 \times 10^{-3}$	Tilt(Y): −6.322 Coma(Y): −3.105	$3A_{21} + 3A_{03} - 2A_{01}$	$1 \times 10^{-3}$	Tilt(X): −6.322 Coma(X): −3.105
9	Spherical	$1 \times 10^{-3}$	Piston: 3.1604 Spherical: −3.146	$6A_{40} + 12A_{22} + 6A_{04} - 6A_{20} - A_{02}$	$1 \times 10^{-3}$	Piston: 3.1446 Spherical: −3.146
10	Trefoil (X)	$1 \times 10^{-3}$	−3.1547	$A_{30} - 3A_{12}$	$1 \times 10^{-3}$	−3.1548
11	Trefoil (Y)	$1 \times 10^{-3}$	−3.1547	$3A_{21} - A_{03}$	$1 \times 10^{-3}$	−3.1548

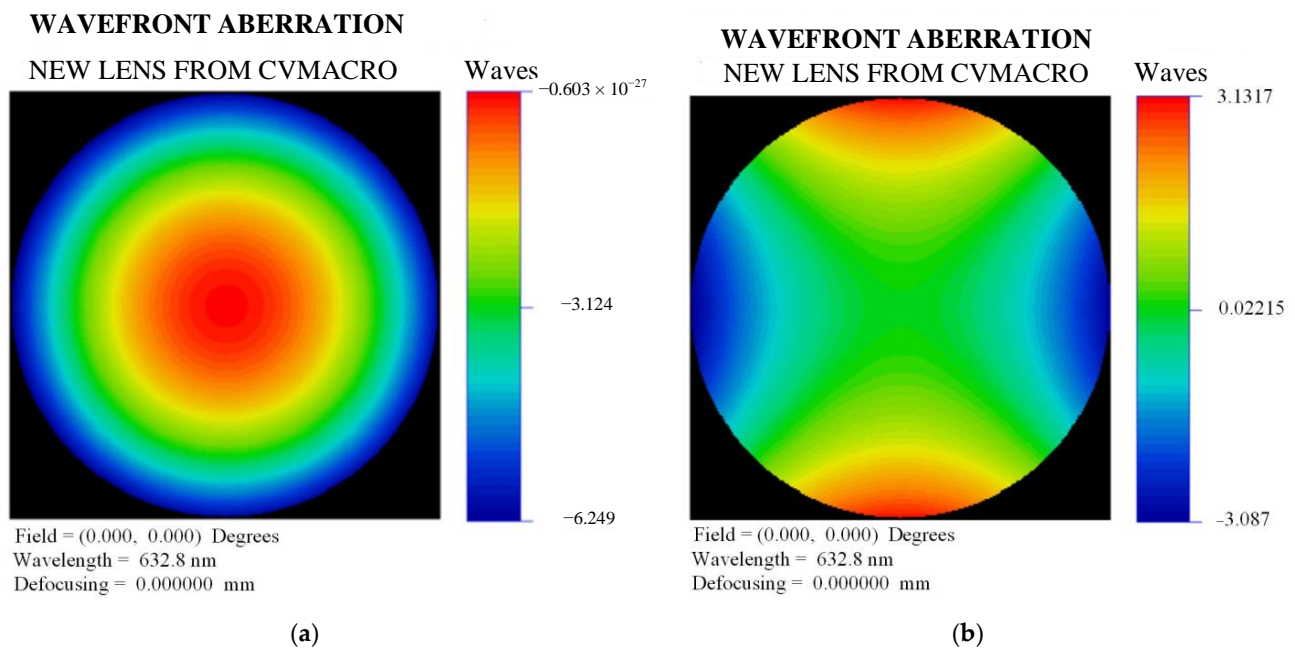


**Figure 3.** The aberration when  $A_{20}$  is positive: (a)  $A_{02}$  with positive value, aberration out of focus; (b)  $A_{02}$  with negative value, aberration-like scattering.

Based on this analysis, the generated aberration of the X–Y polynomial combinations was consistent with the aberration of the Fringe Zernike polynomial, and these two types had the same value, which proved the quantitative relationship between the X–Y free-form surface and the aberration. This was an instructive method for aberration balancing and optical designing based on an X–Y free-form surface. The 3D diagram of the free-form surface is shown in Figure 4. As could be seen from the figure, the free-form surface had a gentle variation, which was suitable for Computer-Generated Hologram (CGH) for mounting and inspection, with less processing difficulty and error, and easy to achieve high inspection accuracy. Therefore, we used the free-form surface described by the X–Y

polynomial in the designed off-axis triple inverse optical system to increase the effective FOV of the system and improve the correction capability of off-axis aberration, especially the correction of off-axis asymmetric aberration.

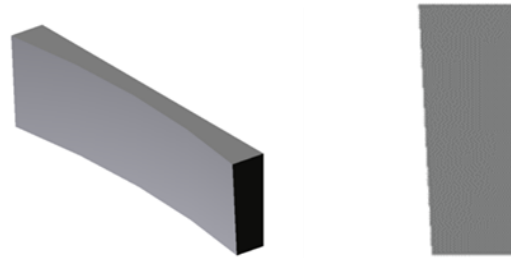


**Figure 4.** Three-dimensional view of the free-form surface.

## 4. System Design and Analysis

### 4.1. Design Results

In this study, we selected the optical simulation software Code V to optimize the aberrations of the TMAS without an intermediate image plane by using the X–Y polynomial surface shape analyzed earlier. In the optimization process, astigmatism and coma were the most important initial aberrations in the parallax field imaging system. Therefore, we selected  $A_{20}$ ,  $A_{02}$ ,  $A_{21}$ ,  $A_{03}$ , and  $A_{01}$  to correct these two aberrations. Throughout the optimization process, the aberration values of the system were controlled. Next, we selected  $A_{40}$ ,  $A_{22}$ , and  $A_{40}$  for spherical aberration correction. Finally, we used other higher-order terms to minimize the RMS wave aberrations in the full FOV. After optimizing the design according to the optical system parameters, we obtained a TMAS with large FOV and low distortion. The optical system structure diagram is shown in Figure 5, the optical path diagram after adding the fold mirror is shown in Figure 6, and the system parameters are given in Table 3. The PM of the system used an X–Y polynomial free-form surface to correct for aberrations in the different FOVs of the system. The system's SM was parabolic, which reduced the difficulty of machining and setting up the system. The TM of the system was an ellipsoidal surface with a high secondary term. To further compress the volume, the focal plane could be folded into the lower part of the TM by adding a fold mirror (400 mm × 52 mm) to the rear intercept of the system. The final optical system had an overall length of  $f'/2.6$ , a height of  $f'/2.9$ , and a width of  $f'/2.25$ , creating a compact system. The configuration parameters are given in Table 4, and the X–Y polynomial of the PM is given in Table 5.

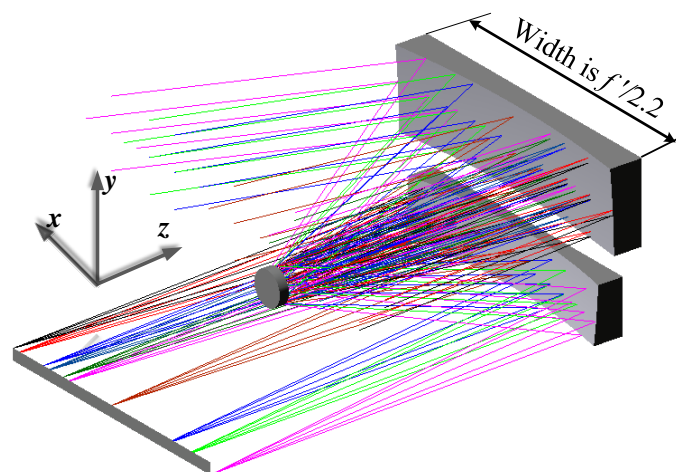


**Figure 5.** Optical system configuration.

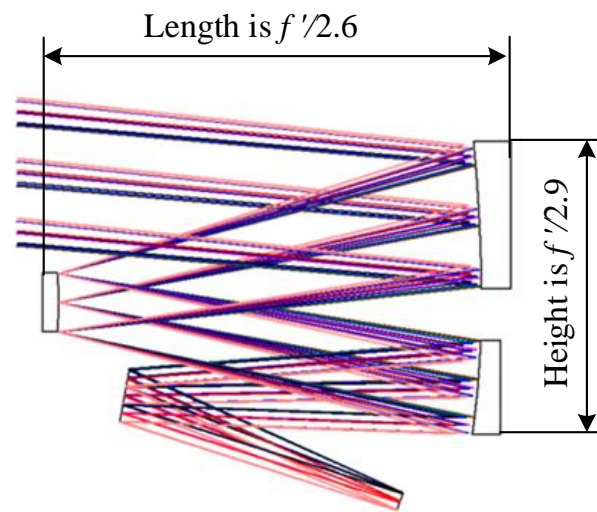


Figure 6. System optical path diagram after adding fold mirror.

Table 3. Parameters of optical system.

No.	Parameter	Value
1	Focal length (mm)	1000
2	F#	9.5
3	FOV (°)	23 × 1
4	Spectrum (nm)	450–850
5	Nyquist frequency (lp/mm)	71.4

Table 4. Configuration parameters of reflective mirror.

Mirror	Surface Type	Radius (mm)	Distance (mm)	Conic	Size (mm)
PM	X–Y polynomial	−1538.978	−384.8	−1.52	444 × 125
SM	Paraboloid	−592.75	384.8	−1	Φ58
TM	Even asphere	−935.58	−648.81	−0.178	392 × 84

Table 5. Polynomial parameters of free-form primary mirror.

No.	Item	$A_{ij}$	No.	Item	$A_{ij}$	No.	Item	$A_{ij}$
1	$X^1Y^0$	0	10	$X^4Y^0$	$2.09 \times 10^{-11}$	19	$X^1Y^4$	0
2	$X^0Y^1$	$-3.97 \times 10^{-4}$	11	$X^3Y^1$	0	20	$X^0Y^5$	$-1.63 \times 10^{-13}$
3	$X^2Y^0$	$-1.41 \times 10^{-7}$	12	$X^2Y^2$	$3.8 \times 10^{-11}$	21	$X^6Y^0$	$-2.98 \times 10^{-17}$
4	$X^1Y^1$	0	13	$X^1Y^3$	0	22	$X^5Y^1$	0
5	$X^0Y^2$	$-1.37 \times 10^{-7}$	14	$X^0Y^4$	$4.47 \times 10^{-11}$	23	$X^4Y^2$	$-7.32 \times 10^{-18}$
6	$X^3Y^0$	0	15	$X^5Y^0$	0	24	$X^3Y^3$	0
7	$X^2Y^1$	$7 \times 10^{-10}$	16	$X^4Y^1$	$-2.01 \times 10^{-14}$	25	$X^2Y^4$	$6.83 \times 10^{-18}$
8	$X^1Y^2$	0	17	$X^3Y^2$	0	26	$X^1Y^5$	0
9	$X^0Y^3$	$-1.39 \times 10^{-9}$	18	$X^2Y^3$	$-2.63 \times 10^{-14}$	27	$X^0Y^6$	$3.4 \times 10^{-16}$

The structural form of the system shows that the TMAC was symmetrical with respect to the  $y$ -axis direction of the meridional plane. To ensure that the imaging quality of the system was symmetrical with respect to the meridional plane, we could not use an expression with odd symmetry for the  $x$ -axis in the design process for optimization. Therefore, we used 13 of the first 28 terms of the  $X$ - $Y$  polynomial as variables to optimize the imaging quality of the system. The  $X$ - $Y$  polynomial expressed as follows:

$$Z = \frac{cr^2}{1 + \sqrt{1 - (1 + k)c^2r^2}} + A_{01}x^0y^1 + A_{20}x^2y^0 + \dots + A_{06}x^0y^6 \tag{4}$$

4.2. Tolerance Analysis

The FOV of the TMAC designed in this paper was  $-11.5^\circ$  to  $+11.5^\circ$  in the arc vector direction and  $-5^\circ$  to  $-6^\circ$  in the meridian direction. We selected 10 FOVs within the effective FOV and evaluated the image quality of the optical system using the operating wavelength of the optical system  $\lambda = 632.8$  nm as the reference wavelength, as shown in Table 6. From the design results, it could be seen that the maximum value of system aberration occurs in the  $(-11.5^\circ, -6^\circ)$  FOV, and the ideal ray tracing position (Parax  $X$ , Parax  $Y$ ) of this FOV was calculated to be  $(-203.597599, -105.18107)$ , and the actual ray tracing position (Real  $X$ , Real  $Y$ ) was  $(-203.4958002, -105.086116)$ . According to the distortion formula where distortion = (real value - ideal value)/ideal value  $\times$  100%, we could get the system in this FOV arc to where the vector direction distortion was  $-0.05\%$ , and the meridian direction distortion was  $0.01\%$ , so the system maximum distortion was  $-0.05\%$ .

Table 6. Field of view (FOV).

No.	$x/(\circ)$	$y/(\circ)$	No.	$x/(\circ)$	$y/(\circ)$
1	0	-5	6	8.05	-5.5
2	5.75	-5	7	11.5	-5.5
3	8.05	-5	8	-5.75	-6
4	11.5	-5	9	-8.05	-6
5	5.75	-5.5	10	-11.5	-6

The MTF is the main parameter used to evaluate the imaging quality of an optical system. As the MTF value increased, the spatial frequency sharpness increased, and the pixel resolution increased. The MTF curve is shown in Figure 7, and the MTF of the system was better than 0.403 at the Nyquist frequency (71.4 lp/mm). The system used a free-form surface to compensate for the asymmetric aberration, which at the same time led to poor uniformity of imaging quality between FOVs. Therefore, the image quality had to be evaluated for the whole FOV. The wave aberration of each FOV is shown in Figure 8, and the maximum wave aberration of the system was  $0.055 \lambda$  ( $\lambda/18.2$ ,  $\lambda = 632.8$  nm), and the system imaging is good. The aberration grid is shown in Figure 9, which is the visual response of the image aberration. As can be seen from the figure, after optimized design, there was basically no deviation between the ideal imaging position and the real image point position. Thus, the aberration was well corrected for the large FOV imaging optical system. Because of the influence of the system phase difference, the light passed through the optical system and presented a diffuse spot on the image surface, and the size of the diffuse spot determined the perfection of the system. As shown in Figure 10, the spot column diagram of each FOV of the system was within the Airy spot, and the imaging quality of the system was completely proportional to the meridional plane. A comprehensive analysis of the data showed that the system had good imaging quality in the effective FOV, and the system had high balance correction capability and low distortion in phase difference. The designed off-axis triple-reverse optical system met the parameters specified in Table 3.

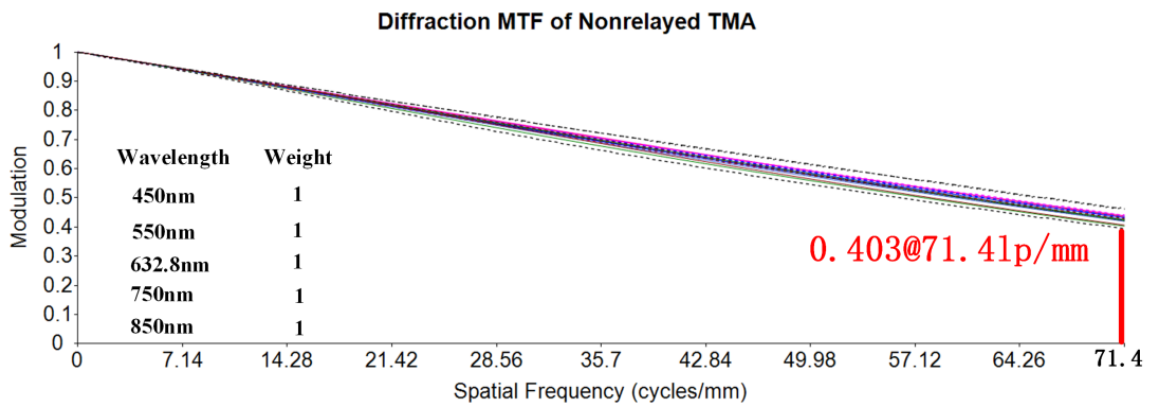


Figure 7. The modulation transfer function (MTF) curves: the dashed line indicates the direction of the arc vector; the solid line indicates the meridian direction.

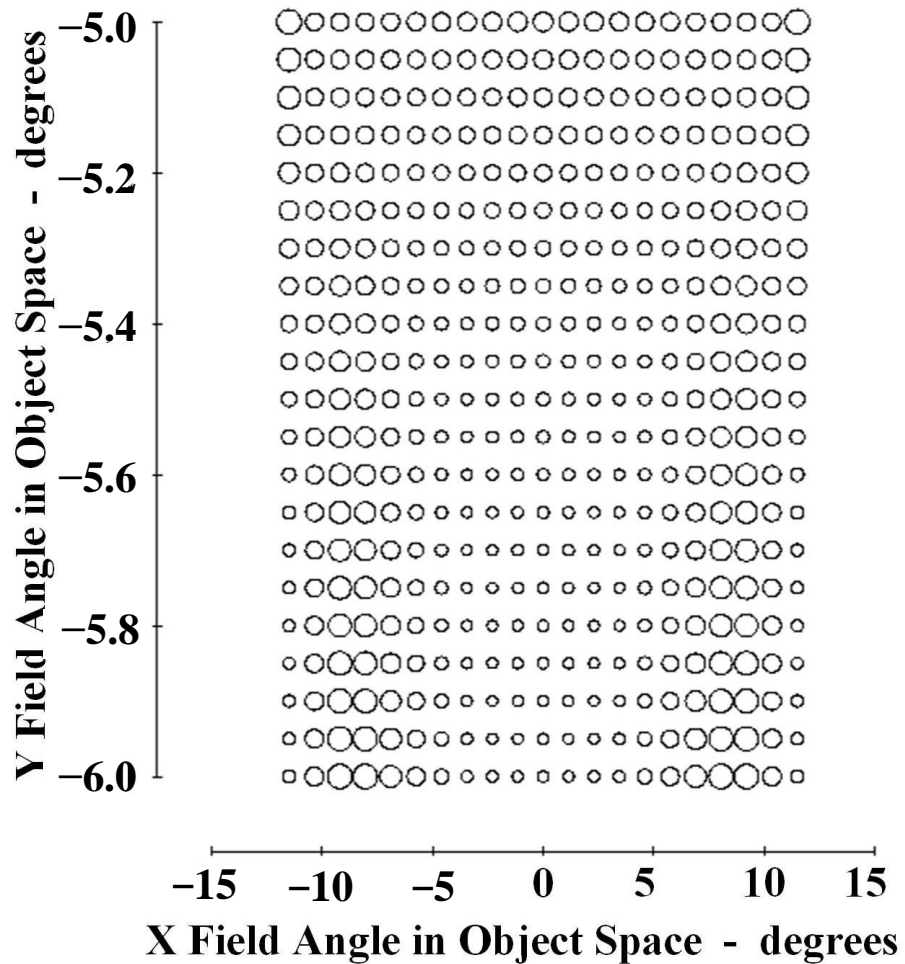


Figure 8. WFE diagram of the system: the wave aberration of each field of view (FOV) is represented by a circle; all points across the FOV are diffraction-limited.

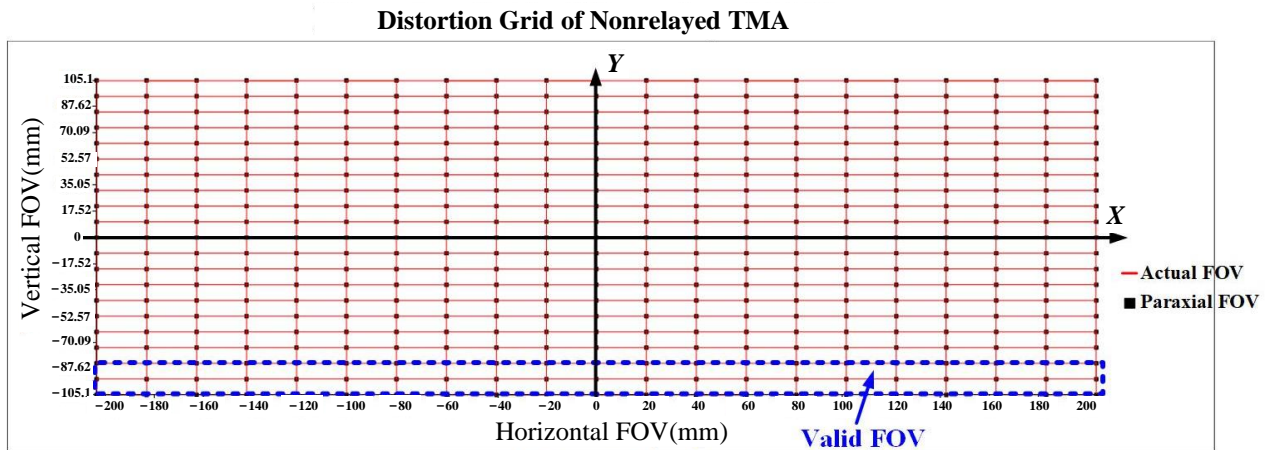


Figure 9. Grid distortion.

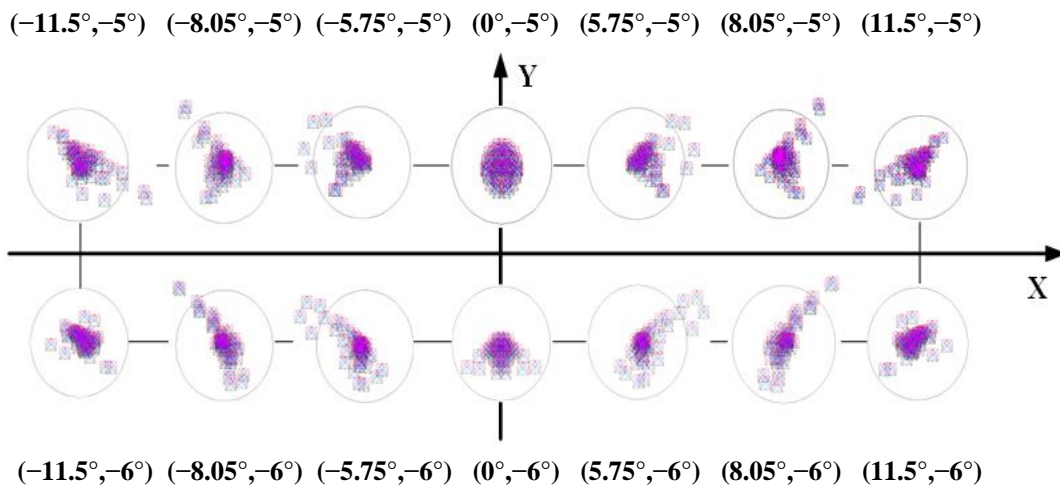


Figure 10. The spot column diagram of each field of view (FOV) of the system.

#### 4.3. System Tolerance Analysis

We analyzed the manufacturing and assembly tolerances of the TMA system using the Monte Carlo method. We used the complex color MTF in Code V software as the performance index and used the FOV in Table 6 as the feature reference point. The image plane position was used as the compensation parameter. The machining tolerances included curvature radius tolerance, secondary surface coefficient tolerance, high secondary aspheric surface tolerance, and face shape tolerance. In the system-mounting process, we used the PM as the reference, and the SM and TM had six DOFs—that is, six position tolerances, including translation and rotation tolerances along the x-, y-, and z-axes. The results of tolerance allocation of the system are shown in Table 7.

After bringing the above tolerances into the optical system, we obtained the MTF curves of different FOVs, as shown in Figure 11. Thus, the results showed that 80% of the MTF was better than 0.37 at Nyquist frequency, and the tolerances were reasonably allocated to meet the design index requirements.

**Table 7.** Tolerance allocation result.

Type	Item	Primary Mirror	Secondary Mirror	Tertiary Mirror
Assembling	Displacement x/mm	-	0.05	0.1
	Displacement y/mm	-	0.05	0.1
	Displacement z/mm	-	0.2	0.3
	Tilt $\alpha$ /(")	-	20	20
	Tilt $\beta$ /(")	-	20	30
	Tilt $\gamma$ /(")	-	40	60
Manufacturing	$\Delta R$ /mm	0.8	0.3	0.3
	$\Delta K$	0.001	0.002	0.001
	Surface error RMS ( $\lambda = 632.8$ nm)	$\lambda/50$	$\lambda/50$	$\lambda/50$

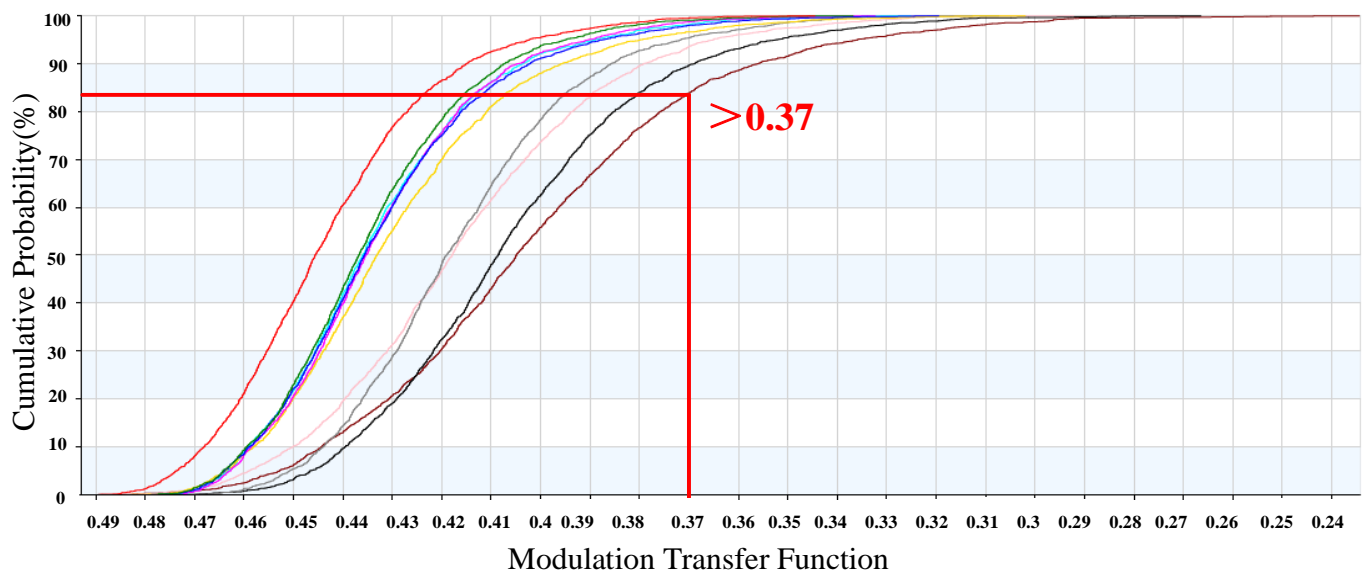


**Figure 11.** Curves of tolerance probability.

### 5. Results and Discussion

In this study, we analyzed and compared the TMAS with an intermediate phase plane and the TMAS without an intermediate image plane. We found that the TMAS without an intermediate image plane was suitable for large FOV imaging, which provided a theoretical basis for the selection of a large FOV imaging optical system design. We verified the relationship between the X–Y polynomial, Fringe-Zernike polynomial, and the aberration based on the quantitative relationship between the X–Y polynomial and aberration. The results provided a guideline for the balance of aberration and the application of the X–Y polynomial free-form surface shapes in optical system design. A three-dimensional diagram of the designed X–Y polynomial free-form surface shape was also created for the purpose of visual observation. Finally, based on the off-axis triple-reversal optical system without an intermediate image plane and the analyzed free-form surface shape, we designed a large FOV low-distortion off-axis triple-reversal optical system with a focal length of 1000 mm, an F-value of 9.5, and an FOV angle of  $23^\circ \times 1^\circ$ . The PM adopted an X–Y polynomial free-form surface to increase the freedom of the system while also correcting the aberration of each FOV. The SM adopted a paraboloidal surface to reduce the difficulty of processing and mounting the system, and the TM was ellipsoidal with a high secondary term. After optimizing the design, the imaging quality of the system

was close to the diffraction limit, the maximum distortion grid in the FOV was less than or equal to  $-0.05\%$ , and the average wave aberration in the whole FOV was better than  $0.055 \lambda$ . Meanwhile, after adding the plane reflector to fold the rear optical path, the total optical length of the system reached  $f'/2.6$ , the height reached  $f'/2.9$ , and the width reached  $f'/2.25$ , creating a compact system structure. The application of the free-form surface expanded the FOV and corrected the system aberrations. After the image quality evaluation and tolerance analysis, we determined that the system achieved good imaging quality. This design method has good application prospects in the design of high-resolution, large FOV, with a long focal length and a light and small push-scan imaging optical load.

**Author Contributions:** Conceptualization, B.J. and Q.L.; methodology, Y.L.; software, Y.L.; validation, B.J., Y.L. and F.J.; formal analysis, Q.L.; investigation, C.T.; resources, C.T.; data curation, F.J.; writing—original draft preparation, Y.L.; writing—review and editing, B.J., Q.L. and C.T.; visualization, Y.L.; supervision, F.J.; project administration, B.J.; funding acquisition, Q.L. All authors have read and agreed to the published version of the manuscript.

**Funding:** This research was funded by the “13th Five-Year Plan” Science and Technology Project of Jilin Provincial Education Department (Grant No. JJKH20200789KJ), Jilin Provincial Science and Technology Department Key R&D Project (Grant No. 20200401120GX), and Changchun University of Science and Technology Project (Grant No. 50923010501).

**Institutional Review Board Statement:** Not applicable.

**Informed Consent Statement:** Not applicable.

**Data Availability Statement:** Not applicable.

**Acknowledgments:** The authors would like to thank the laboratory and university for their support.

**Conflicts of Interest:** The authors declare no conflict of interest.

## References

1. Gorevoy, A.V.; Machikhin, A.S.; Khokhlov, D.D.; Batshev, V.I. Optimization of prism-based stereoscopic imaging systems at the optical design stage with respect to required 3D measurement accuracy. *Opt. Express* **2020**, *28*, 24418–24430. [[CrossRef](#)] [[PubMed](#)]
2. Kim, D.W.; Suratwala, T.I.; Schröder, S. Special Section Guest Editorial: Ultraprecision Optics Fabrication and Characterization. *Opt. Eng.* **2019**, *58*, 092601. [[CrossRef](#)]
3. Yang, T.; Zhu, J.; Wu, X.F.; Jin, G.F. Direct design of freeform surfaces and freeform imaging systems with a point-by-point three-dimensional construction-iteration method. *Opt. Express* **2015**, *23*, 10233–10246. [[CrossRef](#)]
4. Shen, Z.H. Design of Large Field of View Off-axis Three-mirror Reflective Optical System. *Electro. Opt. Technol. Appl.* **2020**, *35*, 24–27, 64. [[CrossRef](#)]
5. Yan, J.H.; Hu, Z.J.; Zhu, D.Y. Design of Compact Off-axis Three-mirror Afocal System Based on Freeform Surface. *Acta Photonica Sin.* **2022**, *51*, 297–307. [[CrossRef](#)]
6. Figoski, J.W. Alignment and test results of the QuickBird telescope using the Ball Optical System Test Facility. *Proc. SPIE* **1999**, *3785*, 99–108. [[CrossRef](#)]
7. Nakajima, M.; Kojima, Y.; Moriyama, T. Mission overview and instrument concept of the Global Imager (GLI). In Proceedings of the SPIE's 1994 International Symposium on Optics, Imaging, and Instrumentation, San Diego, CA, USA, 14 September 1994. [[CrossRef](#)]
8. Mazzoli, A.; Holbrouck, P.; Houbrechts, Y.; Maresi, L.; Stockman, Y.; Taccola, M.; Versluys, J. Baffles design of the PROBA-V wide FOV TMA. In Proceedings of the International Conference on Space Optics—ICSO 2010, Rhodes Island, Greece, 20 November 2017. [[CrossRef](#)]
9. Ohgi, N.; Iwasaki, A.; Kawashima, T.; Inada, H. Japanese hyper-multi spectral mission. In Proceedings of the 2010 IEEE International Geoscience and Remote Sensing Symposium, Honolulu, HI, USA, 25–30 July 2010; pp. 3756–3759. [[CrossRef](#)]
10. Hugot, E.; Wang, X.; Valls-Gabaud, D.; Lemaître, G.; Agócs, T.; Wang, J.Y. A freeform-based, fast, wide-field, and distortion-free camera for ultralow surface brightness surveys. *Proc. SPIE* **2014**, *9143*, 9143X. [[CrossRef](#)]
11. Liu, Y.X.; Zhang, D.D.; Niu, X.H. Design of Multi-spectrum Push-broom optical system. *Opt. Tech.* **2022**, *48*, 139–143. [[CrossRef](#)]
12. Miao, L.; Zhu, L.; Fang, C.; Yan, N.; Yang, X.; Zhang, X. Modeling and Analysis of System Error for Highly Curved Freeform Surface Measurement by Noncontact Dual-Axis Rotary Scanning. *Sensors* **2021**, *21*, 554. [[CrossRef](#)] [[PubMed](#)]
13. Fang, F.Z.; Zhang, X.D.; Weckenmann, A.; Zhang, G.X.; Evans, C. Manufacturing and measurement of freeform optics. *CIRP Ann. Manuf. Technol.* **2013**, *62*, 823–846. [[CrossRef](#)]
14. Chen, S.Y.; Xue, S.; Zhai, D.D.; Tie, G.P. Measurement of Freeform Optical Surfaces: Trade-Off between Accuracy and Dynamic Range. *Laser Photonics Rev.* **2020**, *14*, 1900365. [[CrossRef](#)]

15. Ma, T.; Yu, J.C.; Liang, P.; Wang, C.H. Design of a freeform varifocal panoramic optical system with specified annular center of field of view. *Opt. Express* **2011**, *19*, 3843–3853. [[CrossRef](#)]
16. Zhu, J.; Hou, W.; Zhang, X.D.; Jin, G.F. Design of a low F-number freeform off-axis three-mirror system with rectangular field-of-view. *J. Opt.* **2015**, *17*, 015605. [[CrossRef](#)]
17. Pan, J.W.; Che-Wen, C.; Huang, K.D.; Wu, C.Y. Demonstration of a broad band spectral head-mounted display with freeform mirrors. *Opt. Express* **2014**, *22*, 12785–12798. [[CrossRef](#)]
18. Schober, C.; Beisswanger, R.; Gronle, A.; Pruss, C.; Osten, W. Tilted Wave Fizeau Interferometer for flexible and robust asphere and freeform testing. *Light Adv. Manuf.* **2022**, *3*, 48. [[CrossRef](#)]
19. Schiesser, E.M.; Bauer, A.; Rolland, J.P. Effect of freeform surfaces on the volume and performance of unobscured three mirror imagers in comparison with off-axis rotationally symmetric polynomials. *Opt. Express* **2019**, *27*, 21750–21765. [[CrossRef](#)] [[PubMed](#)]
20. Zhang, B.Q.; Jin, G.F.; Zhu, J. Towards automatic freeform optics design: Coarse and fine search of the three-mirror solution space. *Light Sci. Appl.* **2021**, *10*, 65. [[CrossRef](#)]
21. Ye, G.F.; Chen, L.; Li, X.H.; Yuan, Q.; Gao, Z.S. Review of optical freeform surface representation technique and its application. *Opt. Eng.* **2017**, *56*, 110901. [[CrossRef](#)]
22. Sun, Y.H.; Sun, Y.Q.; Chen, X.Y.; Wang, F.; Yan, X.; Zhang, X.N.; Cheng, T.L. Design of a free-form off-axis three-mirror optical system with a low f-number based on the same substrate. *Appl. Opt.* **2022**, *61*, 7033–7040. [[CrossRef](#)] [[PubMed](#)]
23. Reimers, J.; Bauer, A.; Thompson, K.; Rolland, J. Freeform spectrometer enabling increased compactness. *Light Sci Appl.* **2017**, *6*, e17026. [[CrossRef](#)] [[PubMed](#)]
24. Zhang, X.; Zheng, L.G.; He, X.; Wang, L.G.; Zhang, F.; Yu, S.Q.; Shi, G.W.; Zhang, B.Z.; Liu, Q.; Wang, T.T. Design and fabrication of imaging optical systems with freeform surfaces. *Proc. SPIE* **2012**, *8486*, 46–55. [[CrossRef](#)]
25. Meng, Q.Y.; Wang, W.; Ma, H.T.; Dong, J.H. Easy-aligned off-axis three-mirror system with wide field of view using freeform surface based on integration of primary and tertiary mirror. *Appl. Opt.* **2014**, *53*, 3028–3034. [[CrossRef](#)] [[PubMed](#)]
26. Chang, J.; Weng, Z.C.; Cong, X.J. Design of compact high-resolution optical system for space and stray-light analysis. *Proc. SPIE* **2022**, *4927*, 71–76. [[CrossRef](#)]
27. Ni, D.W.; Li, X.Y.; Ren, Z.G.; Wang, Y.M.; Wang, L.; Tian, C.L. Design of off-axis three-mirror freeform optical system with wide field of view. *Proc. SPIE* **2019**, *10837*, 108370Z. [[CrossRef](#)]
28. Cook, L.G. Three mirror anastigmatic optical system. U.S. Patent 4265510, 5 May 1981.
29. Rodgers, J.M. Unobscured mirror designs. In Proceedings of the International Optical Design Conference 2002, Tucson, AZ, USA, 3–5 June 2002. [[CrossRef](#)]
30. Yang, T.; Ye, Y.Z.; Cheng, D.W. Freeform Imaging Optical System Design: Theories, Development, and Applications. *Acta Opt. Sin.* **2021**, *41*, 0108001. [[CrossRef](#)]
31. Kirschstein, S.; Koch, A.; Schöneich, J.; Döngi, F. Metal mirror TMA, telescopes of Jena spaceborne scanners: Design and analysis. *Proc. SPIE* **2005**, *5962*, 59621M. [[CrossRef](#)]
32. Atchison, D.A.; Scott, D.H.; Cox, M.J. Mathematical treatment of ocular aberrations: A user's guide. In *Vision Science and Its Applications*; Lakshminarayanan, V., Ed.; Optica Publishing Group: Santa Fe, NM, USA, 2000; pp. 110–130. [[CrossRef](#)]

**Disclaimer/Publisher's Note:** The statements, opinions and data contained in all publications are solely those of the individual author(s) and contributor(s) and not of MDPI and/or the editor(s). MDPI and/or the editor(s) disclaim responsibility for any injury to people or property resulting from any ideas, methods, instructions or products referred to in the content.